Applied Catalysis B: Environmental 247 (2019) 49–56

Contents lists available at ScienceDirect

Applied Catalysis B: Environmental

journal homepage: www.elsevier.com/locate/apcatb

Platform for molecular-material dual regulation: A direct Z-scheme MOF/COF heterojunction with enhanced visible-light photocatalytic activity

Sijing He[a,b], Qinfeng Rong[c], Hongyun Niu[a], Yaqi Cai[a,b,d,*]

[a] State Key Laboratory of Environmental Chemistry and Ecotoxicology, Research Center for Eco-Environmental Sciences, Chinese Academy of Sciences, Beijing, 100085, China
[b] University of Chinese Academy of Sciences, Beijing, 100049, China
[c] Key Laboratory of Bio-Inspired Smart Interfacial Science and Technology of Ministry of Education, School of Chemistry, Beihang University, Beijing, 100191, China
[d] Institute of Environment and Health, Jianghan University, Wuhan, 430056, China

ARTICLE INFO

Keywords:
Covalent organic frameworks
Metal-organic frameworks
Heterogeneous photocatalysis
Visible-light-driven
Z-scheme heterojunction

ABSTRACT

Series of novel metal-organic framework/covalent organic framework (MOF/COF) hybrid materials were constructed by encapsulating MOF with highly stable TTB-TTA (a COF synthesized from 4,4′,4″-(1,3,5-triazine-2,4,6-triyl)tribenzaldehyde (TTB) and 4,4′,4″-(1,3,5-triazine-2,4,6-triyl)trianiline (TTA)) layer, inheriting their merits of high crystallinity, large surface area, outstanding visible-light response and tunable band gaps. The introduction of NH_2-MIL-125(Ti) into the hybrid materials could modulate their optical, electronic and redox properties, and promote the charge separation owing to the formation of heterojunction, thus resulting in an enhanced photocatalytic performance for organic pollutant decomposition. As such, NH_2-MIL-125(Ti)/TTB-TTA composite has a much higher photodegradation kinetic of methyl orange (MO) which is over 9 and 2 times the rates of pure NH_2-MIL-125(Ti) and TTB-TTA, respectively. This versatile molecular-material platform can achieve dual adjusting modes consisting of a COF molecular engineering and a MOF type screening strategy, which will be applicable to a wide range of fields.

1. Introduction

Visible-light-responsive photocatalysts can directly harvest energy from solar light, offering a sustainable and prospective pathway to alleviate the energy crisis and environmental issues [1,2]. The central issue of this field is to consider the development of efficient and stable photocatalysts that are capable of harvesting visible light and suppressing charge carrier recombination. Recently, there has been a great surge of interest in visible-light-induced photodegradation of organic pollutants using organic rather than inorganic photocatalysts. The most widely studied organic photocatalytic material is graphitic carbon nitride (g-C_3N_4) which exhibits high chemical stability and an appealing electronic structure [3–9]. Otherwise, some other nitrogen containing organic polymers were also investigated, such as poly(triazine imide) frameworks [10], heptazine-based polymer networks [11–13], hydrazine-based covalent organic frameworks [14], triazine-based frameworks [15–17], triphenyl-azine frameworks [18], or conjugated poly (azomethine) networks [19].

Among them, covalent organic frameworks (COFs), which are porous and crystalline macromolecules with periodic architectures [20–22], have drawn increasing attention in the field of photocatalysis [23–25]. This is because COFs offer a strategy to precisely integrate photocatalytic active units into extended structures with periodic skeletons and ordered nanopores by a highly controlled and predictable manner [26]. In addition, the diversity of building blocks and covalent linkage topology schemes brings rich changes in structural control and functional design. More importantly, its optoelectronic properties and band gaps can be tailored via the selection of appropriate building blocks, linkage motifs, and their stacking mode [27–32]. Based on this, we have precisely controlled COFs structures by assembling the diverse subunits, and further investigated their structure-activity relationship [33]. Fortunately, the obtained COF (TTB-TTA) with richly available active sites and highly delocalized π-system possesses ultrahigh photodegradation efficiency. However, the kind of building units in an identical COF skeleton is very limited due to its structural periodicity, which is difficult to simultaneously fulfill all these requirements for enhancing photocatalytic activity, such as a wide absorption range, large surface area, high charge-separation efficiency, and long-term

* Corresponding author at: State Key Laboratory of Environmental Chemistry and Ecotoxicology, Research Center for Eco-Environmental Sciences, Chinese Academy of Sciences, Beijing, 100085, China.
E-mail address: caiyaqi@rcees.ac.cn (Y. Cai).

https://doi.org/10.1016/j.apcatb.2019.01.078
Received 26 November 2018; Received in revised form 17 January 2019; Accepted 27 January 2019
Available online 01 February 2019
0926-3373/

stability.

To address this problem, an effective strategy is to form proper composites that could create synergistic effect to afford multifunctional properties for photocatalysis. Besides the porosity and stability, the composite materials should make sure the opposite migration of electrons and holes by conduction band (CB) and valence band (VB) offsets [34]. Through deliberate design, a multicomponent heterojunction material can effectively facilitate charge separation and charge carrier transfer, substantially improving photocatalytic and photoelectrochemical efficiency. As a class of porous crystalline materials with large flexibility in design and post-synthetic modification [35–38], metal-organic frameworks (MOFs) are promising candidates for conjugating with COFs [39]. This new type of MOF/COF hybrid materials contribute to providing more possibilities for the structural and functional modulation, and better maintaining their large surface area, inherent porosity and high crystallinity.

Herein, a MOF/COF photocatalytic system featuring the spatial isolation of photogenerated charge carriers was constructed by covalently anchoring a visible-light active COF (TTB-TTA) onto the surface of a MOF. Three common amine-functionalized MOFs, NH_2-MIL-53(Al), NH_2-MIL-125(Ti) and NH_2-UiO-66(Zr), were selected as dopants to form heterogeneous photocatalysts with highly photocatalytic active TTB-TTA. The photoelectric and photocatalytic performance of these three composites were systematically investigated and compared. Thanks to the matching of band gaps between NH_2-MIL-125(Ti) and TTB-TTA, the resulting NH_2-MIL-125(Ti)/TTB-TTA composite with highly accessible surface area, porous framework and high crystallinity exhibited superb photocatalytic activity for organic pollutants degradation under visible light irradiation. A direct Z-scheme heterojunction was generated between NH_2-MIL-125(Ti) and TTB-TTA, wherein the photoinduced electrons in NH_2-MIL-125(Ti) combined with the holes in TTB-TTA, leading to enhanced charge carrier extraction and utilization upon photoexcitation. Additionally, this photocatalyst is fairly stable with cycling due to the encapsulation of COF and the robust connection of covalent bonds. Hence, this design strategy provides a versatile molecular-material platform to construct the heterojunctions for the application in photocatalysis.

2. Experimental section

2.1. Synthesis of MOF/COF hybrid materials

Series of MOF/COF hybrid materials were prepared by adding MOF into the synthetic reaction system of TTB-TTA-COF, which denoted as N/TTB-TTA (N = NH_2-MIL-53(Al), NH_2-MIL-125(Ti) and NH_2-UiO-66(Zr)). In a typical procedure, 0.05 g of as-synthesized MOF, 4,4′,4″-(1,3,5-triazine-2,4,6-triyl)tribenzaldehyde (TTB) (0.25 mmol, 98.3 mg) and 4,4′,4″-(1,3,5-triazine-2,4,6-triyl)trianiline (TTA) (0.25 mmol, 88.6 mg) were dispersed in a ternary solvent mixture of mesitylene/1,4-dioxane/3 M acetic acid (5/5/1 by vol.; 11.0 mL). The reaction mixture was sonicated for 15 min, bubbled with nitrogen for another 15 min, and then heated at 120 °C for 3 days. The resulting precipitate was collected via centrifugation, washed with acetone and THF, and then dried at 120 °C under vacuum overnight. As a result, the binary MOF/TTB-TTA (the mass ratio of MOF to TTB-TTA was 35%) composites were fabricated. The different weights (0.025, 0.05 and 0.075 g) of NH_2-MIL-125(Ti) were added to synthesize the NH_2-MIL-125(Ti)/TTB-TTA composites which were named as NH_2-MIL-125(Ti)$_{0.025}$/TTB-TTA, NH_2-MIL-125(Ti)$_{0.05}$/TTB-TTA and NH_2-MIL-125(Ti)$_{0.075}$/TTB-TTA, respectively. The above naming approach could equally apply to NH_2-MIL-53(Al)/TTB-TTA and NH_2-UiO-66(Zr)/TTB-TTA composites.

2.2. Characterization

The morphology of the synthesized sample was characterized by a Hitachi H-7500 transmission electron microscope (TEM, Tokyo, Japan) and a Zeiss GeminiSEM 300 field-emission scanning electron microscope (SEM, Oberkochen, Germany). Powder X-ray diffraction (PXRD, Almelo, Netherlands) using a Cu Ka radiation ranging from 3° to 60° with a resolution of 0.02° was utilized to analysis the crystallinity. Fourier transform-infrared (FT-IR) spectra were recorded on a NEXUS 670 Infrared Fourier Transform Spectrometer (Nicolet Thermo, Waltham, MA). Solid-state nuclear magnetic resonance (NMR) spectroscopy was obtained on a JNM-ECZ600R spectrometer (JEOL). Thermogravimetric analysis (TGA) was carried out on a TGA Q5000 IR thermogravimetric analyzer (TA Instruments, New Castle, U.S.A.) with the heating rate of 10 °C min^{-1} under N_2 atmosphere. The specific surface area was calculated according to the Brunauer–Emmett–Teller (BET) method. The diffuse reflectance spectra (DRS) were collected using a Hitachi U-3900 UV–vis spectrophotometer ($BaSO_4$ as a reflectance standard). X-ray photoelectron spectroscopy (XPS) was measured with an ESCA-Lab-200i-XL spectrometer (Thermo Scientific, Waltham, MA) with monochromatic Al Kα radiation (1486.6 eV).

2.3. Photoelectrochemical measurements

The measurements were conducted on a CHI660E electrochemical analyzer (Chenhua, Shanghai, China) in a standard three-electrode system, using a platinum foil as the counter electrode and Ag/AgCl (saturated KCl) as the reference electrode. The working electrodes were prepared as follows: 5 mg of photocatalyst powder was dispersed in 1 mL of DMF with 50 μL of Nafion solution (5%) by sonication for 30 min, and then the obtained slurry was dip-coated on the surface of indium tin oxide (ITO) glass substrate. The electrolyte was a 0.1 mol L^{-1} Na_2SO_4 aqueous solution. Electrochemical impedance spectroscopy (EIS) frequency ranged from 1 to 10^6 Hz with an AC voltage magnitude of 10 mV.

2.4. Photocatalytic activity measurement

The photocatalytic activities of the obtained samples were evaluated by the photodegradation of the organic dye methyl orange (MO) and colorless phenol. A 300 W xenon lamp equipped with a UV cutoff filter ($\lambda > 420$ nm) was used as the visible light source. Typically, 15 mg of the photocatalyst powder was dispersed in 50 mL pollutant solution with a concentration of 10 mg L^{-1}. Prior to visible light irradiation, the resultant mixture was stirred in the dark for 1 h to achieve an adsorption–desorption equilibrium. At the given intervals, 3.0 mL of the suspension was withdrawn followed by centrifugation to remove the residual photocatalyst particulates. The concentration of the organic pollutants was analyzed by measuring the maximum absorbance at 462 nm for MO and 270 nm for phenol using a UV–vis spectrophotometer. The mineralization of MO under different irradiation times was studied by a total organic carbon (TOC) analyzer (SHIMADZU).

3. Results and discussion

Using the previously reported solvothermal method [40–42], NH_2-MIL-53(Al), NH_2-MIL-125(Ti) and NH_2-UiO-66(Zr) were prepared, and their amino functional groups were used for covalently linking COF through a convenient condensation reaction. The chemical identity of three resulting MOFs was verified by Fourier transform infrared (FT-IR) spectroscopy and powder X-ray diffraction analysis (see the Supporting Information, Fig. S3 and Fig. S4). Series of MOF/COF hybrid materials were synthesized by introducing as-prepared MOFs into the synthetic reaction system of TTB-TTA (TTB, 4,4′,4″-(1,3,5-triazine-2,4,6-triyl) tribenzaldehyde; TTA, 4,4′,4″-(1,3,5-triazine-2,4,6-triyl)trianiline) without extra functionalization step (Fig. 1). The ^{13}C cross-polarization magic angle spinning nuclear magnetic resonance (CP-MAS NMR) spectra of three hybridized products are almost identical to those of TTB-TTA and their respective MOFs, further confirming the formation of TTB-TTA shell and the structural preservation of MOFs core during

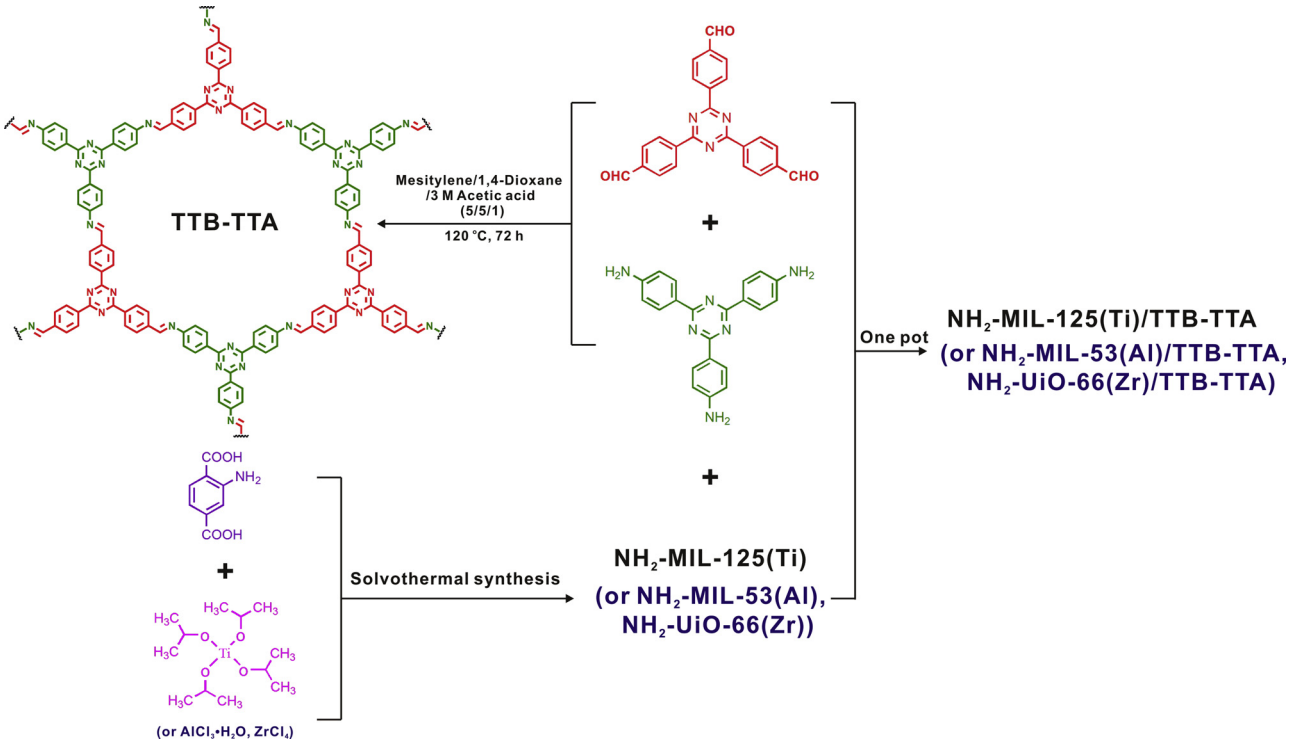

Fig. 1. Schematic illustration of the synthesis of three MOF/COF hybrid materials.

the hybridization process (Fig. S5). As depicted in Fig. S6, the FT-IR spectra of three hybrid materials match well with the TTB-TTA and appear the typical imine (C=N) stretching vibrational bands, indicative of the completion of condensation and the integration of TTB-TTA and MOFs. According to the X-ray photoelectron spectroscopy (XPS) analysis, the content of aluminum, titanium, and zirconium was 3.02%, 2.68%, and 1.35% for NH_2-MIL-53(Al)/TTB-TTA, NH_2-MIL-125(Ti)/TTB-TTA, and NH_2-UiO-66(Zr)/TTB-TTA, respectively. Powder X-ray diffraction (PXRD) indicates the formation of a highly crystalline TTB-TTA COF with well-defined peaks $2\theta = 4.06^{\circ}$, 6.90°, 8.06°, 10.68°, and 25.80° belonging to the (100), (110), (200), (210), and (001) facets, respectively. The PXRD patterns of three MOF/COF composites are similar to TTB-TTA owing to the weak intensity of MOFs, demonstrating that the crystal structure of parent TTB-TTA were well retained (Fig. S7). The high crystallinities of photocatalysts with the declined density of crystal defects can reduce the number of charge carrier recombination sites, thus enhance the charge mobility. In accordance with the above analyses, it can be concluded that series of MOF/TTB-TTA hybrid materials have been successfully fabricated.

These three MOF/COF hybrid materials inherited the excellent thermal stability of COF, as revealed by thermogravimetric analysis, which indicates that less than 10% weight loss occurred up to 350 °C (Fig. S8). The N_2 adsorption isotherms of MOF/COF hybrid materials, measured at 77 K, show reversible type-IV isotherms characteristic of a mesoporous nature (Fig. S9). Brunauer-Emmett-Teller (BET) surface area was 322, 1846 and 1824 $m^2 g^{-1}$ for NH_2-MIL-53(Al)/TTB-TTA, NH_2-MIL-125(Ti)/TTB-TTA and NH_2-UiO-66(Zr)/TTB-TTA, respectively, which is higher than those of pure MOFs, such as NH_2-MIL-53(Al) (38 $m^2 g^{-1}$), NH_2-MIL-125(Ti) (1469 $m^2 g^{-1}$), and NH_2-UiO-66(Zr) (703 $m^2 g^{-1}$), due to the present of TTB-TTA with high surface area (a value of 1903 $m^2 g^{-1}$ was reported previously) [33]. The pore-size distributions were calculated by the nonlocal density functional theory (NLDFT) method, showing that the major population of pore width of the three MOF/COF hybrid materials resides at 2.0 nm which is close to the theoretical pore size of TTB-TTA (2.2 nm) [43]. As displayed in both transmission electron microscopy (TEM) and scanning electron microscopy (SEM) images, the pristine NH_2-MIL-53(Al) (Fig. 2a and g) and NH_2-UiO-66(Zr) (Fig. 2c and i) consist of irregular particles with straight or round edges. After hybridization, it is observed that NH_2-MIL-53(Al) and NH_2-UiO-66(Zr) particles are decorated on the TTB-TTA sheets, respectively, and their interfacial contact is intimate (Fig. 2d and j and Fig. 2f and l). In Fig. 2h, NH_2-MIL-125(Ti) presents as monodispersed disc-like particles with smooth surface. Distinct from NH_2-MIL-53(Al)/TTB-TTA and NH_2-UiO-66(Zr)/TTB-TTA products, NH_2-MIL-125(Ti)/TTB-TTA composite has the tendency to produce a core-shell morphology, wherein the sheet-like TTB-TTA wrapped on the surface of NH_2-MIL-125(Ti) particles and then sprouted the thorn-like structure (Fig. 2e and k).

The photocatalytic performances of the synthesized samples were evaluated by measuring the decomposition rate of the model contaminants (MO dye and colorless phenol) under visible light irradiation, as shown in Fig. 3. Without the present of a photocatalyst, the self-photolysis of MO can be negligible under visible light exposure. Before photocatalytic tests, photocatalysts were fully contacted with pollutants to ensure the adsorption-desorption equilibrium. In both Fig. 3a and Fig. S10, NH_2-MIL-125(Ti)/TTB-TTA exhibits superior MO photodegradation capacity compared to the parent NH_2-MIL-125(Ti) and TTB-TTA, and other MOF/COF hybrid materials, as evidenced by the characteristic absorbance of MO at 462 nm declined rapidly within 20 min illumination (Fig. 3b). However, for the NH_2-MIL-125(Ti) + TTB-TTA physical mixture, its photocatalytic activity was far worse than that of the composite (Fig. 3c). This was due to the prominent role of covalent connection in hybrid material, which could improve photogenerated electron transfer in the heterojunction [44]. The photodegradation kinetics were fitted to a pseudo-first-order reaction, $-\ln(C/C_0) = kt$, where k is the apparent rate constant. As can be seen in Fig. 3d, after coupled with NH_2-MIL-125(Ti), the photocatalytic capacities of the series of NH_2-MIL-125(Ti)/TTB-TTA hybrid materials exhibit distinct increase tendency compared with the parent TTB-TTA. Among them, the NH_2-MIL-125(Ti)$_{0.05}$/TTB-TTA possesses the maximum photodegradation efficiency with an apparent rate constant of 0.20 min^{-1}, which is above 9-folds and 2-folds higher than those of the

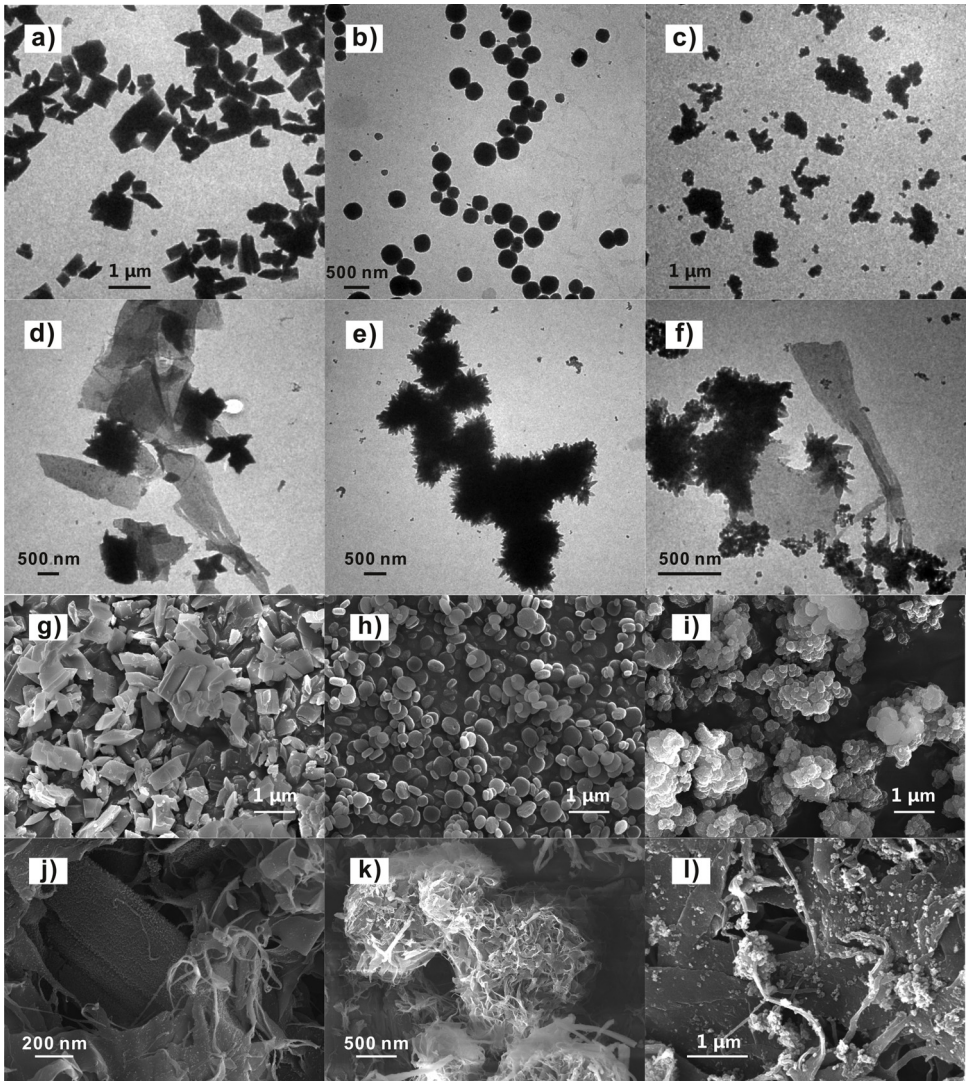

Fig. 2. TEM images of three MOFs (NH_2-MIL-53(Al) (a), NH_2-MIL-125(Ti) (b) and NH_2-UiO-66(Zr) (c)) and three MOF/COF hybrid materials (NH_2-MIL-53(Al)/TTB-TTA (d), NH_2-MIL-125(Ti)/TTB-TTA (e) and NH_2-UiO-66(Zr)/TTB-TTA (f)), and SEM images of three MOFs (NH_2-MIL-53(Al) (g), NH_2-MIL-125(Ti) (h) and NH_2-UiO-66(Zr) (i)) and three MOF/COF hybrid materials (NH_2-MIL-53(Al)/TTB-TTA (j), NH_2-MIL-125(Ti)/TTB-TTA (k) and NH_2-UiO-66(Zr)/TTB-TTA (l)).

pure NH_2-MIL-125(Ti) (0.021 min^{-1}) and TTB-TTA (0.086 min^{-1}), respectively. Conversely, the photocatalytic efficiencies of hybrid materials were slightly reduced by incorporating equal mass of NH_2-MIL-53(Al) and NH_2-UiO-66(Zr). After optimizing the mass ratios of NH_2-MIL-53(Al) and NH_2-UiO-66(Zr) to TTB-TTA in the hybrid materials, respectively, the resulting photocatalytic performances still cannot transcend that of NH_2-MIL-125(Ti)/TTB-TTA (Fig. S11), which indicates that it is crucial to integrate the suitable component with well-matched band structure into the hybrid material. With the optimum photocatalyst NH_2-MIL-125(Ti)$_{0.05}$/TTB-TTA, 27.9% of mineralization of MO is reached after 20 min irradiation under visible light. Furthermore, considering the sensitization effect, a colorless organic compound, phenol, has also been utilized for photodegradation studies. As presented in Fig. 3e, similar photodegradation trends were achieved with phenol: the photocatalytic activities are in the consistent order of NH_2-MIL-125(Ti) + TTB-TTA physical mixture < NH_2-UiO-66(Zr)/TTB-TTA < NH_2-MIL-53(Al)/TTB-TTA < TTB-TTA < NH_2-MIL-125(Ti)/TTB-TTA.

To better understand the origin of photocatalytic activity of MOF/COF composites, it is necessary to deeply investigate their optical and electronic properties. Fig. 4a shows the optical properties of as-prepared pure TTB-TTA and three MOF/TTB-TTA samples, as measured by UV–vis diffuse reflectance spectra (DRS). The pristine TTB-TTA has an absorption edge at around 496 nm, corresponding to the band gap of 2.50 eV. Benefiting from the incorporation of MOFs, the absorption edges of three hybrid composites were found to red shift with slightly enhanced absorption in the visible-light region, suggesting that the presence of MOFs in hybrids is effective for the visible-light response to varying degrees. The band gap energies (*Eg*) are estimated to be 2.76, 2.46 and 2.71 eV for NH_2-MIL-53(Al), NH_2-MIL-125(Ti) and NH_2-UiO-66(Zr), respectively (Fig. S12). Based on the valence band X-ray photoelectron spectra (VB XPS) from Fig. 4b, the valence band (VB) edges of TTB-TTA, NH_2-MIL-53(Al), NH_2-MIL-125(Ti) and NH_2-UiO-66(Zr) are located at 2.15, 3.58, 3.23 and 3.25 eV, respectively. As determined by the equation of $E_{CB} = E_{VB} - E_g$, their corresponding conduction band (CB) potentials are calculated to be –0.35, 0.82, 0.77 and 0.54 eV, respectively. Therefore, from the electronic band alignments of four polymers in Fig. 4c, we can infer that the hybridization with NH_2-MIL-125(Ti) is conducive to narrow the band gap and positive-shift the VB position. The efficient generation, migration, and separation of photo-induced electron-hole pairs are prerequisite to initiate photocatalysis, which can be analyzed by photocurrent response and electrochemical impedance spectroscopy (EIS). As is evident from Fig. S13, NH_2-MIL-125(Ti) produces a much higher photocurrent density than the other

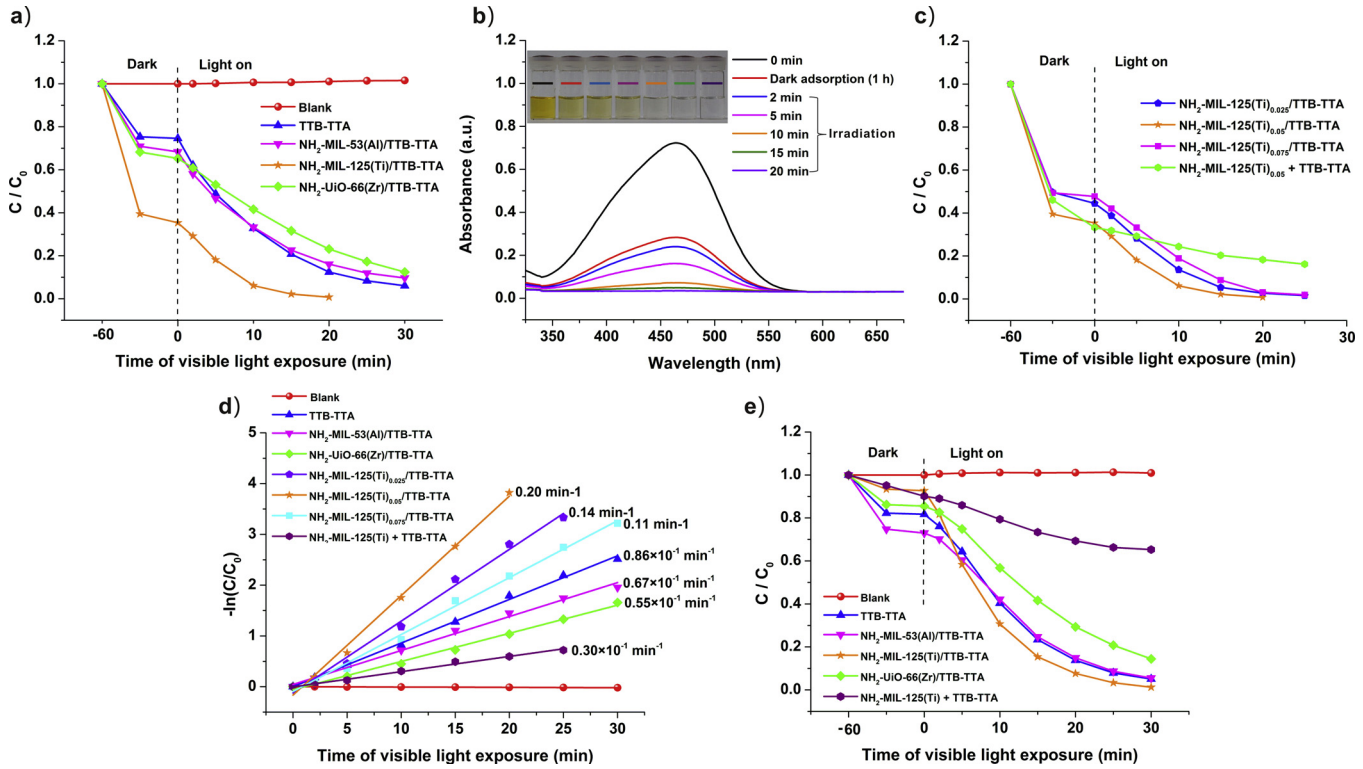

Fig. 3. (a) Photocatalytic degradation of MO (10 mg L^{-1}) over as-prepared photocatalysts under visible light irradiation. (b) UV–vis absorption spectra of MO under different irradiation times by using NH_2-MIL-125(Ti)/TTB-TTA. (c) Photocatalytic degradation of MO over NH_2-MIL-125(Ti)/TTB-TTA hybrid materials with different mass ratios and different hybrid approaches. (d) Kinetics linear simulation curves of MO photodegradation over different photocatalysts. (e) Photodegradation of phenol (10 mg L^{-1}) over TTB-TTA, NH_2-MIL-53(Al)/TTB-TTA, NH_2-MIL-125(Ti)/TTB-TTA, NH_2-UiO-66(Zr)/TTB-TTA, and the physical mixture of NH_2-MIL-125(Ti) and TTB-TTA (NH_2-MIL-125(Ti) + TTB-TTA).

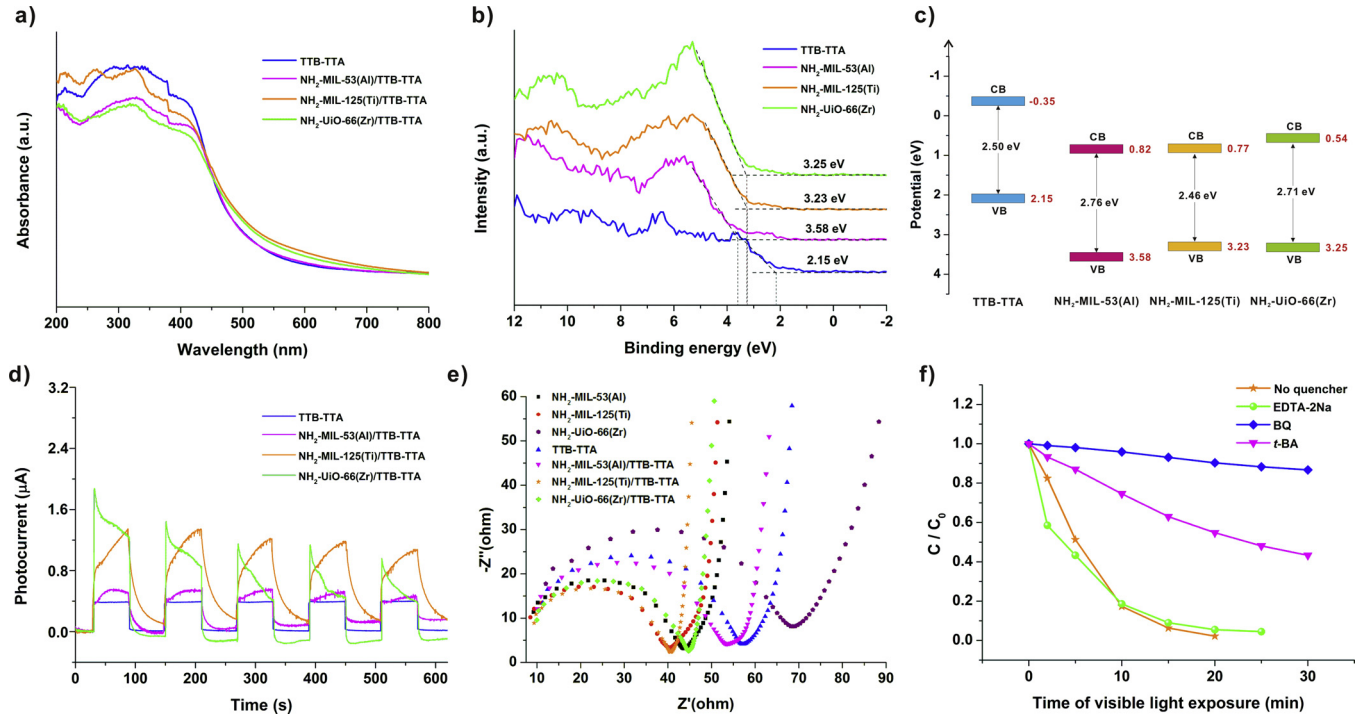

Fig. 4. (a) UV–vis diffuse reflectance spectra of TTB-TTA, NH_2-MIL-53(Al)/TTB-TTA, NH_2-MIL-125(Ti)/TTB-TTA and NH_2-UiO-66(Zr)/TTB-TTA. (b) VB XPS spectra, and (c) band alignment of TTB-TTA, NH_2-MIL-53(Al), NH_2-MIL-125(Ti) and NH_2-UiO-66(Zr). (d) Photocurrent responses, and (e) EIS Nyquist plots of TTB-TTA, NH_2-MIL-53(Al)/TTB-TTA, NH_2-MIL-125(Ti)/TTB-TTA and NH_2-UiO-66(Zr)/TTB-TTA. (f) Photodegradation of MO over NH_2-MIL-125(Ti)/TTB-TTA with different scavengers, C_0 is the initial concentration of MO after dark adsorption tests.

two MOFs under visible light. The transient photocurrent responses of TTB-TTA, NH_2-MIL-53(Al)/TTB-TTA, NH_2-MIL-125(Ti)/TTB-TTA and NH_2-UiO-66(Zr)/TTB-TTA with several on-off cycles of intermittent visible light irradiation are shown in Fig. 4d. After doping TTB-TTA, the photocurrent intensities of binary MOF/COF composites were significantly enhanced with respect to the individual MOF, which could be ascribed to a more efficient photogenerated charge transfer in the extend conjugation of COF by aromatic rings incorporation. However, under prolonged illumination, photocurrents of NH_2-MIL-53(Al)/TTB-TTA and NH_2-UiO-66(Zr)/TTB-TTA appeared conspicuous decays. On the contrary, the photocurrent response of NH_2-MIL-125(Ti)/TTB-TTA is steady and reversible, being over 16 and 2 times higher than those of the parent NH_2-MIL-125(Ti) and TTB-TTA, respectively. In Fig. 4e, the EIS Nyquist plots show that NH_2-MIL-125(Ti)/TTB-TTA possesses the smallest arc radius among the samples studied, strongly implying the highest electron transfer efficiency and the smallest interfacial resistance. Taken together, the addition of NH_2-MIL-125(Ti) to TTB-TTA not only improves the light-harvesting ability but also facilitates charge mobility and separation, thereby endowing NH_2-MIL-125(Ti)/TTB-TTA composite with the most potent photocatalytic performance.

To elucidate the photocatalytic mechanism of NH_2-MIL-125(Ti)/TTB-TTA composite, the radical trapping experiments were performed to investigate the roles of active species in photocatalysis. The sacrificial agents, including *p*-benzoquinone (BQ), *tert*-butanol (*t*BA), and ethylenediaminetetraacetic acid disodium salt (EDTA-2Na) were added as the scavengers for superoxide radicals ($O_2^{\cdot -}$), hydroxyl radicals ($OH^{\cdot}$) and holes (h^+), respectively. As shown in Fig. 4f, a significant suppression of dye molecules decomposition is observed with the existence of BQ or *t*BA, which confirms the crucial roles of $O_2^{\cdot -}$ and $OH^{\cdot}$ in the degradation process. Conversely, the photocatalytic kinetics is accelerated after adding EDTA-2Na. This may be attributed to the effect that the competitive reaction of excess holes with EDTA-2Na decreased the recombination rate, leading to more available excess electrons for oxidative radical-mediated degradation [45]. All these results manifest that under visible light excitation, generated charge carriers induced the formation of reactive oxygen species, which are responsible for the photodegradation process with the main contribution from $O_2^{\cdot -}$ and $OH^{\cdot}$.

On the basis of their band structures and the radical trapping experiments, the underlying photocatalytic mechanism for the pollutant degradation over NH_2-MIL-125(Ti)/TTB-TTA hybrid material has been proposed. Once exposed to the illumination by photons of energy exceeding (or equal to) the bandgap, both NH_2-MIL-125(Ti) and TTB-TTA can be excited to generate electron-hole pairs. If the photogenerated charge carrier transfers via conventional type-II heterojunction mechanism (Fig. 5a), the conduction band electrons of TTB-TTA are transferred to CB of NH_2-MIL-125(Ti), meanwhile, valence band holes of NH_2-MIL-125(Ti) are moved to VB of TTB-TTA. This charge transfer mechanism results in weakened redox ability of electrons and holes, and thermodynamical detriment for the photocatalytic reactions. Due to the positive CB edge potential of NH_2-MIL-125(Ti) (0.77 eV), electrons in the CB of NH_2-MIL-125(Ti) cannot reduce O_2 into $O_2^{\cdot -}$ radicals with the standard redox potential of O_2/ $O_2^{\cdot -}$ (−0.33 eV), which is not in agreement with the obtained results. In contrast, according to the direct Z-scheme heterojunction mechanism in Fig. 5b, the photoinduced electrons in the CB of NH_2-MIL-125(Ti) migrated to the VB of TTB-TTA and recombined with the holes, leading to effective spatial charge separation. The accumulated electrons in the CB of TTB-TTA are trapped by the dissolved oxygen to yield $O_2^{\cdot -}$ radicals participating in the photodecomposition. Besides, considering the holes in the VB of NH_2-MIL-125(Ti) possess the stronger oxidizability power than those of TTB-TTA, $OH^{\cdot}$ radicals would be more likely to be formed by the Z-scheme electron transfer mode rather than the conventional type-II heterojunction. Eventually, these highly oxidative species ($O_2^{\cdot -}$ and $OH^{\cdot}$ radicals) can efficiently degrade and mineralize organic pollutants. The contaminant degradation in the NH_2-MIL-125(Ti)/TTB-TTA system is believed to follow the Z-scheme carrier transfer model, which enabled the photocatalyst to simultaneously possess high charge-separation efficiency and strong redox ability [46].

In addition to the high photocatalytic activity, the durability and stability of photocatalyst is also closely related to its practical application. Fig. S14 displays the cyclic stability tests of synthesized photocatalyst under visible light irradiation. Impressively, NH_2-MIL-125(Ti)/TTB-TTA maintained a photocatalytic ability of 85.1% after repeated cycling, strongly indicating that it can be efficiently recycled and reused without appreciable deterioration. No noticeable alternations have been found, either in the chemical structure or in the morphology of MOF/COF composite after the pollutant photodecomposition, as supported by FT-IR and TEM analysis (Fig. S15 and Fig. S16). The highly stable COF shell covering the MOF core can effectively protect the composite against photocorrosion and deactivation. Additionally, the robust covalent bond between these two species further guarantees the excellent stability of the multi-components photocatalytic system.

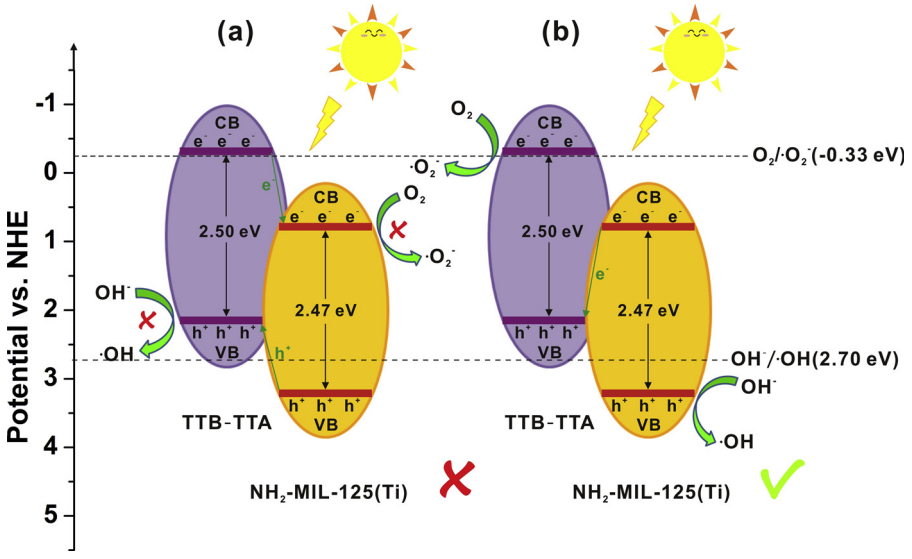

Fig. 5. Type-II heterojunction (a) and Z-scheme (b) charge-transfer mechanisms for the NH_2-MIL-125(Ti)/TTB-TTA system.

4. Conclusions

In summary, a series of covalently integrated MOF/COF hybrid materials were designed and synthesized, and employed as visible-light-active photocatalysts for water decontamination. Compared with other MOF/COF hybrid systems, the resulting NH_2-MIL-125(Ti)/TTB-TTA exhibits superior visible light photocatalytic ability in eliminating organic pollutants due to the ideal band matching and effectively promoting the charge separation across the covalent heterojunction interface. Moreover, the COF encapsulation and the covalent connecting junction render the NH_2-MIL-125(Ti)/TTB-TTA composite extremely stable. On the basis of the detected active oxidant species, the charge transfer follows a direct Z-scheme mechanism, which not only preserves the strong redox ability of photogenerated electron–hole pairs but also isolates them spatially. Therefore, we anticipate that these well-connected hybrid molecular-material platforms can be further extended to a broad range of practical implementations.

Acknowledgments

This work was supported by the National Key Research and Development Program (2016YFA0203100), the National Natural Science Foundation of China (21537004, 21621064, 21777169), and the Strategic Priority Research Program of the Chinese Academy of Sciences (XDB14010201).

Appendix A. Supplementary data

Supplementary material related to this article can be found, in the online version, at doi:https://doi.org/10.1016/j.apcatb.2019.01.078.

References

[1] C. Chen, W. Ma, J. Zhao, Semiconductor-mediated photodegradation of pollutants under visible-light irradiation, Chem. Soc. Rev. 39 (2010) 4206–4219.
[2] D. Chatterjee, S. Dasgupta, Visible light induced photocatalytic degradation of organic pollutants, J. Photochem. Photobiol. C: Photochem. Rev. 6 (2005) 186–205.
[3] Z. Tong, D. Yang, Z. Li, Y. Nan, F. Ding, Y. Shen, Z. Jiang, Thylakoid-inspired multishell g-C_3N_4 nanocapsules with enhanced visible-light harvesting and electron transfer properties for high-efficiency photocatalysis, ACS Nano 11 (2017) 1103–1112.
[4] X. Yang, F. Qian, G. Zou, M. Li, J. Lu, Y. Li, Facile fabrication of acidified g-C_3N_4/g-C_3N_4 hybrids with enhanced photocatalysis performance under visible light irradiation, Appl. Catal. B: Environ. 193 (2016) 22–35.
[5] Y. Wang, H. Wang, F. Chen, F. Cao, X. Zhao, S. Meng, Y. Cui, Facile synthesis of oxygen doped carbon nitride hollow microsphere for photocatalysis, Appl. Catal. B: Environ. 206 (2017) 417–425.
[6] J. Li, B. Shen, Z. Hong, B. Lin, B. Gao, Y. Chen, A facile approach to synthesize novel oxygen-doped g-C_3N_4 with superior visible-light photoreactivity, Chem. Commun. 48 (2012) 12017–12019.
[7] X. Wang, K. Maeda, A. Thomas, K. Takanabe, G. Xin, J.M. Carlsson, K. Domen, M. Antonietti, A metal-free polymeric photocatalyst for hydrogen production from water under visible light, Nat. Mater. 8 (2009) 76–80.
[8] X. Wang, X. Chen, A. Thomas, X. Fu, M. Antonietti, Metal-containing carbon nitride compounds: a new functional organic–metal hybrid material, Adv. Mater. 21 (2009) 1609–1612.
[9] W. Wang, T. An, G. Li, D. Xia, H. Zhao, J.C. Yu, P.K. Wong, Earth-abundant Ni_2P/g-C_3N_4 lamellar nanohydrids for enhanced photocatalytic hydrogen evolution and bacterial inactivation under visible light irradiation, Appl. Catal. B: Environ. 217 (2017) 570–580.
[10] L. Lin, C. Wang, W. Ren, H. Ou, Y. Zhang, X. Wang, Photocatalytic overall water splitting by conjugated semiconductors with crystalline poly(triazine imide) frameworks, Chem. Sci. 8 (2017) 5506–5511.
[11] K. Kailasam, J. Schmidt, H. Bildirir, G. Zhang, S. Blechert, X. Wang, A. Thomas, Room temperature synthesis of heptazine-based microporous polymer networks as photocatalysts for hydrogen evolution, Macromol. Rapid Commun. 34 (2013) 1008–1013.
[12] K. Kailasam, M.B. Mesch, L. Möhlmann, M. Baar, S. Blechert, M. Schwarze, M. Schröder, R. Schomäcker, J. Senker, A. Thomas, Donor–acceptor-type heptazine-based polymer networks for photocatalytic hydrogen evolution, Energy Technol. 4 (2016) 744–750.
[13] H. Ou, X. Chen, L. Lin, Y. Fang, X. Wang, Biomimetic donor–acceptor motifs in conjugated polymers for promoting exciton splitting and charge separation, Angew. Chem. Int. Ed. 57 (2018) 8729–8733.
[14] L. Stegbauer, K. Schwinghammer, B.V. Lotsch, A hydrazone-based covalent organic framework for photocatalytic hydrogen production, Chem. Sci. 5 (2014) 2789–2793.
[15] L. Li, W. Fang, P. Zhang, J. Bi, Y. He, J. Wang, W. Su, Sulfur-doped covalent triazine-based frameworks for enhanced photocatalytic hydrogen evolution from water under visible light, J. Mater. Chem. A 4 (2016) 12402–12406.
[16] J. Bi, W. Fang, L. Li, J. Wang, S. Liang, Y. He, M. Liu, L. Wu, Covalent triazine-based frameworks as visible light photocatalysts for the splitting of water, Macromol. Rapid Commun. 36 (2015) 1799–1805.
[17] P. Yang, R. Wang, M. Zhou, X. Wang, Photochemical construction of carbonitride structures for red-light redox catalysis, Angew. Chem. Int. Ed. 57 (2018) 8674–8677.
[18] V.S. Vyas, F. Haase, L. Stegbauer, G. Savasci, F. Podjaski, C. Ochsenfeld, B.V. Lotsch, A tunable azine covalent organic framework platform for visible light-induced hydrogen generation, Nat. Commun. 6 (2015) 8508.
[19] M.G. Schwab, M. Hamburger, X. Feng, J. Shu, H.W. Spiess, X. Wang, M. Antonietti, K. Müllen, Photocatalytic hydrogen evolution through fully conjugated poly (azomethine) networks, Chem. Commun. 46 (2010) 8932–8934.
[20] S.-Y. Ding, W. Wang, Covalent organic frameworks (COFs): from design to applications, Chem. Soc. Rev. 42 (2013) 548–568.
[21] X. Feng, X. Ding, D. Jiang, Covalent organic frameworks, Chem. Soc. Rev. 41 (2012) 6010–6022.
[22] P.J. Waller, F. Gándara, O.M. Yaghi, Chemistry of covalent organic frameworks, Acc. Chem. Res. 48 (2015) 3053–3063.
[23] P. Pachfule, A. Acharjya, J. Roeser, T. Langenhahn, M. Schwarze, R. Schomäcker, A. Thomas, J. Schmidt, Diacetylene functionalized covalent organic framework (COF) for photocatalytic hydrogen generation, J. Am. Chem. Soc. 140 (2018) 1423–1427.
[24] S. He, Q. Rong, H. Niu, Y. Cai, Construction of a superior visible-light-driven photocatalyst based on a C_3N_4 active centre-photoelectron shift platform-electron withdrawing unit triadic structure covalent organic framework, Chem. Commun. 53 (2017) 9636–9639.
[25] T. Sick, A.G. Hufnage, J. Kampmann, I. Kondofersky, M. Calik, J.M. Rotter, A. Evans, M. Döblinger, S. Herbert, K. Peters, D. Böhm, P. Knochel, D.D. Medina, D. Fattakhova-Rohlfing, T. Bein, Oriented films of conjugated 2D covalent organic frameworks as photocathodes for water splitting, J. Am. Chem. Soc. 140 (2018) 2085–2092.
[26] M. Calik, F. Auras, L.M. Salonen, K. Bader, I. Grill, M. Handloser, D.D. Medina, M. Dogru, F. Löbermann, D. Trauner, A. Hartschuh, T. Bein, Extraction of photogenerated electrons and holes from a covalent organic framework integrated heterojunction, J. Am. Chem. Soc. 136 (2014) 17802–17807.
[27] S. Wan, J. Guo, J. Kim, H. Ihee, D. Jiang, A belt-shaped, blue luminescent, and semiconducting covalent organic framework, Angew. Chem. Int. Ed. 47 (2008) 8826–8830.
[28] E.L. Spitler, J.W. Colson, F.J. Uribe-Romo, A.R. Woll, M.R. Giovino, A. Saldivar, W.R. Pichtel, Lattice expansion of highly oriented 2D phthalocyanine covalent organic framework films, Angew. Chem. Int. Ed. 51 (2012) 2623–2627.
[29] Z.-A. Lan, Y. Fang, Y. Zhang, X. Wang, Photocatalytic oxygen evolution from functional triazine-based polymers with tunable band structures, Angew. Chem. Int. Ed. 57 (2018) 470–474.
[30] G. Lin, H. Ding, R. Chen, Z. Peng, B. Wang, C. Wang, 3D porphyrin-based covalent organic frameworks, J. Am. Chem. Soc. 139 (2017) 8705–8709.
[31] T. Sick, A.G. Hufnagel, J. Kampmann, I. Kondofersky, M. Calik, J.M. Rotter, A. Evans, M. Döblinger, S. Herbert, K. Peters, D. Böhm, P. Knochel, D.D. Medina, D. Fattakhova-Rohlfing, T. Bein, Oriented films of conjugated 2D covalent organic frameworks as photocathodes for water splitting, J. Am. Chem. Soc. 140 (2018) 2085–2092.
[32] X. Chen, M. Addicoat, E. Jin, L. Zhai, H. Xu, N. Huang, Z. Guo, L. Liu, S. Irle, D. Jiang, Locking covalent organic frameworks with hydrogen bonds: general and remarkable effects on crystalline structure, physical properties, and photochemical activity, J. Am. Chem. Soc. 137 (2015) 3241–3247.
[33] S. He, B. Yin, H. Niu, Y. Cai, Targeted synthesis of visible-light-driven covalent organic framework photocatalyst via molecular design and precise construction, Appl. Catal. B: Environ. 239 (2018) 147–153.
[34] R. Marschall, Semiconductor composites: strategies for enhancing charge carrier separation to improve photocatalytic activity, Adv. Funct. Mater. 24 (2014) 2421–2440.
[35] H.-C. Zhou, S. Kitagawa, Metal–organic frameworks (MOFs), Chem. Soc. Rev. 43 (2014) 5415–5418.
[36] W. Lu, Z. Wei, Z.-Y. Gu, T.-F. Liu, J. Park, J. Park, J. Tian, M. Zhang, Q. Zhang, G. Thomas III, M. Bosch, H.C. Zhou, Tuning the structure and function of metal–organic frameworks via linker design, Chem. Soc. Rev. 43 (2014) 5561–5593.
[37] Y. Cui, B. Li, H. He, W. Zhou, B. Chen, G. Qian, Metal－organic frameworks as platforms for functional materials, Acc. Chem. Res. 49 (2016) 483–493.
[38] P. Yao, H. Liu, D. Wang, J. Chen, G. Li, T. An, Enhanced visible-light photocatalytic activity to volatile organic compounds degradation and deactivation resistance mechanism of titania confined inside a metal-organic framework, J. Colloid Interface Sci. 522 (2018) 174–182.
[39] M. Wen, G. Li, H. Liu, J. Chen, T. An, H. Yamashita, Metal-organic frameworks-based nanomaterials for adsorption and photocatalytic degradation of gaseous pollutants: recent progress and challenges, Environ. Sci. Nano (2018), https://doi.org/10.1039/c8en01167b in press.
[40] T. Rodenas, M.V. Dalen, E. Garcia-Perez, P. Serra-Crespo, B. Zornoza, F. Kapteijn, J. Gascon, Visualizing MOF mixed matrix membranes at the nanoscale: towards structure-performance relationships in CO_2/CH_4 separation over NH_2- MIL-53(Al)@PI, Adv. Funct. Mater. 24 (2014) 249–256.
[41] M.A. Nasalevich, R. Becker, E.V. Ramos-Fernandez, S. Castellanos, S.L. Veber,

M.V. Fedin, F. Kapteijn, J.N.H. Reek, J.I. van der Vlugt, J. Gascon, Co@NH_2-MIL-125(Ti): cobaloxime-derived metal–organic framework-based composite for light-driven H_2 production, Energy Environ. Sci. 8 (2015) 364–375.

[42] L. Shen, S. Liang, W. Wu, R. Liang, L. Wu, CdS-decorated UiO–66(NH_2) nanocomposites fabricated by a facile photodeposition process: an efficient and stable visible-light-driven photocatalyst for selective oxidation of alcohols, J. Mater. Chem. A 1 (2013) 11473–11482.

[43] P. Wang, Q. Xu, Z. Li, W. Jiang, Q. Jiang, D. Jiang, Exceptional iodine capture in 2D covalent organic frameworks, Adv. Mater. 30 (2018) 1801991–1801997.

[44] F.-M. Zhang, J.-L. Sheng, Z.-D. Yang, X.-J. Sun, H.-L. Tang, M. Lu, H. Dong, F.-C. Shen, J. Liu, Y.-Q. Lan, Rational design of MOF/COF hybrid materials for photocatalytic H_2 evolution in the presence of sacrificial electron donors, Angew. Chem. 130 (2018) 12282–12286.

[45] S. Ghosh, N.A. Kouamé, L. Ramos, S. Remita, A. Dazzi, A. Deniset-Besseau, P. Beaunier, F. Goubard, P.-H. Aubert, H. Remita, Conducting polymer nanostructures for photocatalysis under visible light, Nat. Mater. 14 (2015) 505–511.

[46] P. Zhou, J. Yu, M. Jaroniec, All-solid-state Z-scheme photocatalytic systems, Adv. Mater. 26 (2014) 4920–2935.